

Diff-CL: A Novel Cross Pseudo-Supervision Method for Semi-supervised Medical Image Segmentation

Xiuzhen Guo^a, Lianyuan Yu^a, Ji Shi^{b,*}, Na Lei^{c,*}, Hongxiao Wang^b

^a*School of Mathematical Science, Capital Normal University, Beijing, 100048, Beijing, China*

^b*Academy for Multidisciplinary Studies, Capital Normal University, Beijing, 100048, Beijing, China*

^c*International Information and Software Institute, Dalian University of Technology, Beijing, 116024, Dalian, China*

Abstract

Semi-supervised learning utilizes insights from unlabeled data to improve model generalization, thereby reducing reliance on large labeled datasets. Most existing studies focus on limited samples and fail to capture the overall data distribution. We contend that combining distributional information with detailed information is crucial for achieving more robust and accurate segmentation results. On the one hand, with its robust generative capabilities, diffusion models (DM) learn data distribution effectively. However, it struggles with fine detail capture, leading to generated images with misleading details. Combining DM with convolutional neural networks (CNNs) enables the former to learn data distribution while the latter corrects fine details. While capturing complete high-frequency details by CNNs requires substantial computational resources and is susceptible to local noise. On the other hand, given that both labeled and unlabeled data come from the same distribution, we believe that regions in unlabeled data similar to overall class semantics to labeled data are likely to belong to the same class, while regions with minimal similarity are less likely to. This work introduces a semi-supervised medical image segmentation framework from the distribution perspective (Diff-CL). Firstly, we propose a cross-pseudo-supervision learning

*Corresponding authors.

Email addresses: xiuzhenguo589@gmail.com (Xiuzhen Guo), lianyuanyu8@gmail.com (Lianyuan Yu), shiji@cnu.edu.cn (Ji Shi), nalei@dlut.edu.cn (Na Lei), hwang21@cnu.edu.cn (Hongxiao Wang)

mechanism between diffusion and convolution segmentation networks. Secondly, we design a high-frequency mamba module to capture boundary and detail information globally. Finally, we apply contrastive learning for label propagation from labeled to unlabeled data. Our method achieves state-of-the-art (SOTA) performance across three datasets, including left atrium, brain tumor, and NIH pancreas datasets.

Keywords: Medical Image Segmentation, Semi-supervised Learning, Diffusion model, Contrastive Learning

1. Introduction

Nowadays, medical image segmentation algorithms plays an important role in computer-assisted medical diagnosis. Image segmentation algorithms based on deep learning are state-of-the-art (SOTA) approaches and obtain good segmentation performance by training abundant labeled data. Medical images usually have characteristics of complex backgrounds and blurred boundaries, which greatly increase the difficulty of labeling, so it is not realistic to obtain a large number of labeled medical data. Semi-supervised learning attempts to make full use of both labeled and unlabeled data to improve the performance of the model.

In general, semi-supervised medical image segmentation methods include consistency regularization (Luo et al. (2021, 2022); Li et al. (2020); Yu et al. (2019); Xu et al. (2023); Gao et al (2023)), pseudo-labeling (Wu et al. (2021, 2022); Rajchl et al. (2017); Bai et al. (2017); Tang et al. (2017); Zhou et al. (2019); Xia et al. (2020); Peng et al. (2020); Dong-DongChen et al (2018); Zhao et al. (2023)), adversarial learning (Lei et al. (2023); Peng et al. (2020)), and graph-based methods (Song et al. (2009); Xu et al. (2016)). Among them, the pseudo-labeling technique leverages the model to predict pseudo-labels for unlabeled data to train the model further. Bai et al. (2017) and Tang et al. (2017) combined the post-processing methods of conditional random fields (CRF) and the level set to refine pseudo-labels, respectively. Rajchl et al. (2017) used weak boundary annotations to assist the supervision process. Zhao et al. (2023) used contrastive learning to optimize the model. Some studies used multiple models to optimize the training process jointly. Zhou et al. (2019) defined an additional student model in a co-training framework. Peng et al. (2020) used the mean of predictions from multiple models as pseudo-labels and introduced adversarial samples to capture differences

between models. [Dong-DongChen et al \(2018\)](#) suggested employing two sub-nets to generate pseudo-labels for a third subnet. These advanced studies have greatly improved the quality of pseudo-labels, however, a limited understanding of data and an inability to learn data distributions when using CNNs as architectures, resulting in poor generalization.

In contrast, diffusion models is a SOTA generative model that can learn data distribution based on finite data. There are some studies for medical image segmentation utilizing diffusion models ([Yao et al. \(2024\)](#); [Peng et al. \(2023\)](#); [Liu et al. \(2023, 2024\)](#)). Some studies have employed diffusion models to generate synthetic images to expand the training dataset ([Yao et al. \(2024\)](#); [Peng et al. \(2023\)](#)). Other studies use diffusion models to characterize existing data. [Liu et al. \(2024\)](#) used latent diffusion models to align pseudo-label distributions across different levels to improve their quality, while [Liu et al. \(2023\)](#) utilized diffusion models as encoders to extract distribution-invariant features. However, diffusion models tend to focus more on learning the data distribution, often at the expense of fine details, which can result in the generation of inaccurate or misleading details.

CNNs typically focus on the details of samples. However, two main limitations arise: first, due to the restricted size of convolutional kernels, they capture only local details, making them vulnerable to local noise and lacking the ability to capture global structures. Second, capturing comprehensive high-frequency details with CNNs requires significant computational resources, which is not ideal for efficient model optimization. Mamba, conceptualized through a state-space model (SSM) ([Wang et al. \(2023\)](#); [Gu et al. \(2023a\)](#); [Gu \(2023b\)](#)), captures long-range dependencies and operates with linear complexity, focusing on global learning of samples to enhance the overall understanding of the model. This architecture has been increasingly used in medical image segmentation, like Segmamba [Xing et al. \(2024\)](#), VM-UNet [Ruan et al. \(2024\)](#), Weak-Mamba-UNet [Wang et al. \(2024\)](#), SliceMamba [Fan et al \(2024\)](#), and skinMamba [Zou et al. \(2024\)](#). Medical images often contain temporal or spatial relationships, making Mamba particularly well-suited for segmentation tasks that involve such structurally coherent data.

Unlabeled data, due to the lack of labels, pose a limitation for existing semi-supervised learning algorithms in effectively learning from them. Most existing methods for learning from unlabeled samples focus solely on the samples themselves, neglecting their relationship with labels. Recently, some works considered the issue [Seibold et al. \(2022\)](#); [Gao et al \(2023\)](#); [Isken et al. \(2019\)](#); [Yang et al. \(2023\)](#) and have a unified point that semantic similar

regions between labeled and unlabeled data may contain the same semantics due to they come from the same distribution and their labels should be shared. Some of them used cosine similarity measurement [Seibold et al. \(2022\)](#) and the construction of an omni-correlation consistency matrix [Gao et al \(2023\)](#) to find similar regions between labeled and unlabeled data. [Iscen et al. \(2019\)](#) treated data points as nodes in a graph, with labeled and unlabeled data connected by edges. Labels propagated between nodes through edges in the graph. [Yang et al. \(2023\)](#) proposed a prototype feature constraint module to constrain pixel features of unlabeled images by prototype features of labeled images, and feature alignment of the whole dataset was realized. These studies effectively provide a novel label information propagation perspective from labeled to unlabeled data. However, local semantic similarities they believed may exist across different labeled classes, making it hard to assign a class to an unlabeled region.

Inspired by these advanced works, we propose a novel semi-supervised medical image segmentation framework from the distribution perspective (Diff-CL). Firstly, Diffusion models effectively characterize the overall data distribution, but may generate images with misleading details. While integrating it with CNNs can enhance model generalization and ensure accurate detail representation. Secondly, (1) Mamba can leverage its ability to incorporate global contextual information, helping to mitigate the limitations of CNNs, which often focus heavily on local details and are prone to being affected by local noise. (2) While CNNs require substantial computational resources to capture high-frequency information, Mamba operates with linear computational complexity, making it well-suited for efficiently capturing high-frequency features. Thirdly, most existing label propagation methods focus on local semantic similarity, but such similarity can exist across different labeled classes, making it difficult to assign a class to an unlabeled region. However, in medical images, the semantic differences between classes are usually significant. Therefore, we believe that regions in unlabeled data similar to overall class semantics in labeled data are likely to belong to the same class, while regions with minimal similarity are less likely to. Our contributions include:

- we propose a diffusion segmentation (DS) and convolution segmentation (CS) cross-pseudo-supervision learning mechanism and design a 3D high-frequency Mamba module to learn high-frequency details globally in medical images.

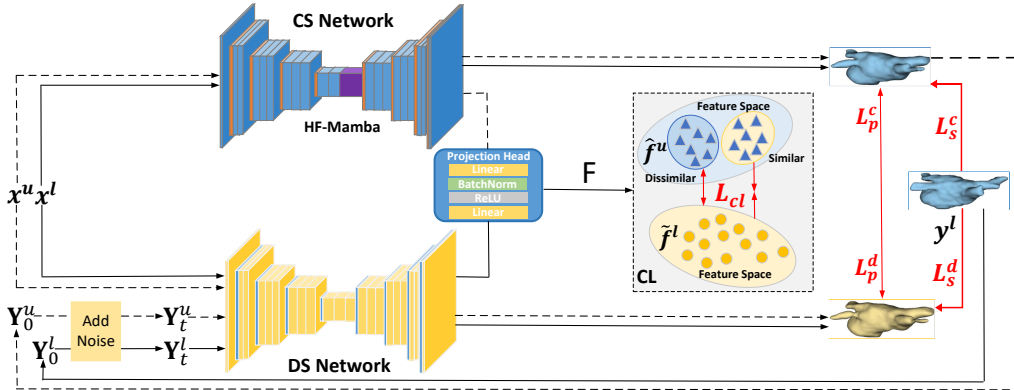


Figure 1: The overall overview of Diff-CL. The backbone consists of CS and DS networks with a projection head. HF-Mamba is our high-frequency mamba module. x^l and x^u are labeled and unlabeled data. y^l is the label of labeled data. $Y_0^l = y^l$ and Y_0^u is the pseudo-label of x^u from CS network. After adding t -step Gaussian noise, we get Y_t^l and Y_t^u . (x^l, Y_t^l) and (x^u, Y_t^u) are concatenated as inputs of DS network. (\hat{f}^l, \hat{f}^u) are labeled and unlabeled features from DS and CS networks respectively. Inter-CL represents inter-sample contrastive learning which closes similar features and pushes dissimilar features away between \hat{f}^l and \hat{f}^u . There are supervised and unsupervised losses. The supervised loss includes L_s^c and L_s^d . The unsupervised loss includes cross pseudo-supervision losses L_p^c and L_p^d and inter-sample contrastive learning loss L_{cl} .

- A new label information propagation method from labeled to unlabeled data utilizing contrastive learning.
- Experimental results on MR and CT datasets demonstrate that Diff-CL significantly improves model generalization.

The paper is organized as follows. Section 2 reviews related works. Section 3 gives preliminaries of Diff-CL needed. Section 4 introduces our method in detail. Section 5 presents experiment results on four medical image datasets. Section 6 is a summary of our whole research.

2. Related Works

We introduce the diffusion model and contrastive learning methods for semi-supervised medical image segmentation and mamba-based methods for medical image segmentation.

2.1. Diffusion Model Methods

Yao et al. (2024) used a latent diffusion model to generate synthetic medical images, reducing the burden of data annotation and addressing privacy issues associated with medical data collection. Liu et al. (2024) introduced a latent diffusion label correction model (DiffRect) for semi-supervised medical image segmentation. A Latent Feature Rectification (LFR) module is applied in the latent space, leveraging latent diffusion to align pseudo-label distributions at different levels. It uses a denoising network to learn continuous distribution transitions from coarse to fine. Peng et al. (2023) employed an implicit diffusion model (LDM) to generate new scleral images. Liu et al. (2023) proposed an aggregation and decoupling framework, where the aggregation part constructs a common knowledge set using a diffusion encoder to extract distribution-invariant features from multiple domains. The decoupling part, consisting of three decoders, separates the training process for labeled and unlabeled data, thus preventing overfitting to labeled data, specific domains, or classes.

Different from them, we propose a dual DS-CS cross pseudo-supervision learning mechanism. The DS network learns the data distribution while the CS network provides detailed calibration. When learning data distribution, DM tends to reconstruct the global structure and main features of the data rather than the details, so the recovery of details may be insufficient. CNNs focus on details of samples. Therefore, the architecture of combining DM and CNNs complements each other.

2.2. Mamba-based Methods

Many studies have explored applications of Mamba in medical image segmentation. Weak-Mamba-UNet Wang et al. (2024) combined CNN-based UNet Ronneberger et al. (2015) for detailed local feature extraction, a Swin Transformer-based SwinUNet Liu et al. (2021) for comprehensive global context understanding, and a VMamba-based Mamba-UNet Liu et al. (2024) for efficient long-range dependency modeling. SliceMamba Fan et al (2024) introduced a Bidirectional Slice Scanning (BSS) module with a specific mechanism, enhancing the ability of Mamba to model local features. SkinMamba Zou et al. (2024) introduced the Frequency Boundary Guided Module (FBGM) to achieve high-frequency restoration and boundary prior guidance. However, these methods are not specifically designed for 3D medical image segmentation. SegMamba Xing et al. (2024) introduced a Three-directional Mamba

(ToM) module to enhance sequential modeling of 3D features from three different directions.

Unlike them, we develop a 3D high-frequency Mamba module for capturing high-frequency details by leveraging global contextual information. Medical images often exhibit structured anatomical patterns with a clear sequential relationship, where global context plays a key role in improving the extraction of fine details.

2.3. Contrastive Learning methods

Contrastive learning is to learn distinctive feature representations by increasing the margin between different classes in the feature space, thus facilitating the distinction between positive and negative pairs. Pixel contrastive learning has been widely adopted for semi-supervised segmentation tasks (Zhong et al. (2021); You et al. (2022); Lai et al. (2021); Zhao et al. (2023); Basak et al (2023)). Zhong et al. (2021) introduced pixel contrastive learning with confidence sampling into consistency training for semi-supervised segmentation. Lai et al. (2021) proposed generating two different views from the same input, encouraging consistency in overlapping regions while establishing bidirectional contrast in other regions. Zhao et al. (2023) introduced a bidirectional voxel contrastive learning strategy to tackle insufficient class separability. This strategy further optimized the model to improve class separability by pulling voxels of the same class closer in feature space while pushing apart those of different classes. Basak et al (2023) designed a Pseudo-label Guided Contrastive Loss (PLGCL) to leverage contrastive learning in capturing important class-discriminative features.

In contrast, we use contrastive learning to propagate label information from labeled to unlabeled data by narrowing the boundaries between regions in the unlabeled data similar to the class overall semantics of labeled data, and expanding the boundaries between unrelated regions. This enhances the intra-class similarity and inter-class separability of the unlabeled data.

3. Preliminaries

For completeness and readability, we introduce the knowledge of diffusion model and Mamba in this section.

3.1. Denoising Diffusion Implicit Models (DDIM)

As a variant of diffusion models, DDIM Song et al. (2020) includes a forward noise-adding process and an accelerated reverse denoising process. The forward process of diffusion models is to define a forward Markov chain of Gaussian transitions, which gradually adds noise to the data x_0 , defined as follows:

$$x_t = \sqrt{\bar{\alpha}_t} \cdot x_0 + \sqrt{1 - \bar{\alpha}_t} \cdot \epsilon, \quad \epsilon \in \mathcal{N}(0, 1), \quad (1)$$

where x_0 is the original data, and t is the diffusion timestep. $\bar{\alpha}_t = \prod_{i=1}^t \alpha_i$ and α_t is a predefined time-dependent scalar.

In DDIM, the reverse denoising process significantly reduces the number of required steps while still achieving high-quality sample generation. The reverse process of DDIM :

$$x_{\tau_{i-1}} = \sqrt{\alpha_{\tau_{i-1}}} x_0 + \sqrt{1 - \alpha_{\tau_i}} \cdot \frac{x_{\tau_i} - \sqrt{\alpha_{\tau_i}} x_0}{\sqrt{1 - \alpha_{\tau_i}}}, \forall i \in [S], \quad (2)$$

where τ_i is a sub-sequence of $[1, \dots, T]$ of length S with $\tau_S = T$. Compared to traditional diffusion models that predict noise ϵ_θ , DDIM allows the network to predict the image x_0 directly, given by:

$$x_0 = \frac{x_t - \sqrt{1 - \bar{\alpha}_t} \epsilon_\theta(x_t, t)}{\sqrt{\bar{\alpha}_t}}. \quad (3)$$

This approach enables the model to generate samples deterministically without conducting iterative noise prediction.

3.2. Mamba

For the convenience of readers, we present the definition of Mamba. Mamba Gu et al. (2023a) is built on the selective state space model (SSM). It is characterized by parameters, \bar{A} , \bar{B} , and C , and transforms a given input sequence $(x_t)_{t=1}^T$ into an output sequence of the same size $(y_t)_{t=1}^T$ via the following equations:

$$\begin{aligned} h_t &= \bar{A}_t h_{t-1} + \bar{B}_t x_t \\ y_t &= C_t h_t \end{aligned} \quad (4)$$

where the initial state $h_0 = 0$. What distinguishes the selective SSM from the original SSM (S4) Gu et al. (2022) is that the evolution parameter, \bar{A}_t , and projection parameters, \bar{B}_t and C_t , are functions of the input x_t . This

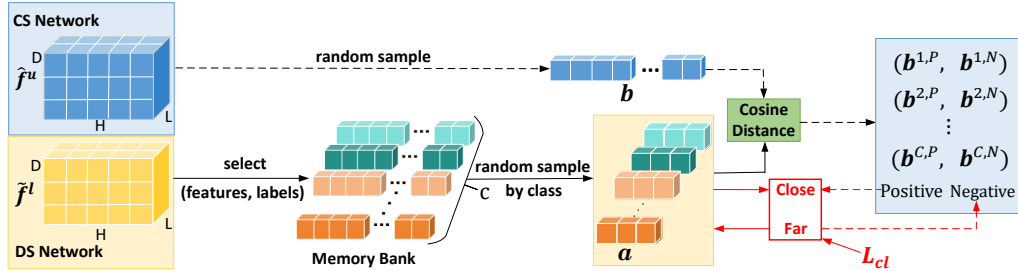


Figure 2: \tilde{f}^l and \hat{f}^u are labeled and unlabeled features output by DS and CS networks respectively. C is the class number of a dataset. \mathbf{a} and \mathbf{b} are randomly sampled feature vectors from our memory bank and \hat{f}^u , respectively. By calculating cosine distances between \mathbf{a} and \mathbf{b} , we get unlabeled positive and negative pairs $\mathbf{b}^{\gamma,P}$ and $\mathbf{b}^{\gamma,N}$ of \mathbf{a} , where $\gamma \in (1, \dots, C)$. L_{cl} is the inter-sample contrastive loss.

enables dynamic adaptation of the SSM’s parameters based on input. This mechanism dynamicity facilitates the model focusing on relevant information while ignoring irrelevant details when processing a sequence.

4. Methodology

Our overall framework is shown in Fig. 1. The proposed Diff-CL has dual DS-CS networks as our backbone that includes a diffusion segmentation network $\tilde{F}(\cdot)$ and a convolutional segmentation network $\hat{F}(\cdot)$. A projection head is used after DS and CS networks to derive labeled features \tilde{f}^l and unlabeled features \hat{f}^u , respectively. The dimension of features is d . In this section, we first present our dual DS-CS cross-pseudo-supervision mechanism in section 4.1, and the high-frequency Mamba module in section 4.2. Then our label propagation method by contrastive learning is explained in section 4.3. Finally, semi-supervised training is detailed in section 4.4.

4.1. DS-CS Cross-Pseudo-Supervision Learning

DS-CS With the specially designed, cross-pseudo-supervised learning means that pseudo-labels of DS provide CS distribution information, and pseudo-labels of CS provide DS correct details.

CS A mini-batch of data inputs in one forward pass including m labeled samples $\{x_i^l\}_{i=1}^m$ and n unlabeled samples $\{x_j^u\}_{j=1}^n$. Softmax outputs of CS for them are denoted as $\hat{P}^l = \{\hat{P}_i^l\}_{i=1}^m$ and $\hat{P}^u = \{\hat{P}_j^u\}_{j=1}^n$. Pseudo-labels of

Table 1: Notations. (the same hereinafter)

Dataset	
$S = S^l \cup S^u$	Dataset
$S^l = \{x_i^l, y_i^l\}_{i=1}^M$	Labeled dataset
$S^u = \{x_j^u\}_{j=1}^N$	Unlabeled dataset
$\{x_i^l, x_j^u, y_i^l\} \in R^{H \times L \times D}$	Dimension of data
C	Class number of one dataset
Network	
$\tilde{F}(\cdot)$	DS network
$\hat{F}(\cdot)$	CS network
F	Projection head
\tilde{f}^l	Labeled features output by our projection head
\hat{f}^u	Unlabeled features output by our projection head
\hat{Y}^u	Pseudo-labels of unlabeled samples predicted by CS network
\tilde{Y}^u	Pseudo-labels of unlabeled samples predicted by DS network
Label propagation by contrastive learning	
$\mathbf{a} = (\mathbf{a}^1, \mathbf{a}^2, \dots, \mathbf{a}^C)$, where $\mathbf{a}^\gamma = (a_1^\gamma, a_2^\gamma, \dots, a_p^\gamma)$, $\gamma \in \{1, \dots, C\}$	Randomly sampled labeled feature vector from DS
$\mathbf{b} = (b_1, b_2, \dots, b_q)$	Randomly sampled unlabeled feature vector from CS

the softmax outputs are denoted as $\hat{Y}^l = \{\hat{Y}_i^l\}_{i=1}^m$ and $\hat{Y}^u = \{\hat{Y}_j^u\}_{j=1}^n$.

DS DS diffuses labels with samples as the condition. However, there is no label for unlabeled data. We replace it with pseudo-labels \hat{Y}^u obtained from CS. To get inputs of DS, first, $y^l = \{y_i^l\}_{i=1}^m$ and \hat{Y}^u are converted into one-hot forms, denoted as Y_0^l and Y_0^u , which serve as the initial clean labels of DS. Next, successive t-step noise ϵ are added to them to obtain noise labels:

$$Y_t^{l/u} = \sqrt{\bar{\alpha}_t} Y_0^{l/u} + \sqrt{1 - \bar{\alpha}_t} \epsilon, \epsilon \in \mathcal{N}(0, 1), \quad (5)$$

where $\bar{\alpha}_t$ is described in 3.1. Finally, (x^l, Y_t^l) and (x^u, Y_t^u) are concatenated as inputs of DS. Softmax outputs of DS for them are denoted as $\tilde{P}^l = \left\{ \tilde{P}_i^l \right\}_{i=1}^m$ and $\tilde{P}^u = \left\{ \tilde{P}_j^u \right\}_{j=1}^n$. Pseudo-labels of the softmax outputs are denoted as $\tilde{Y}^l = \left\{ \tilde{Y}_i^l \right\}_{i=1}^m$ and $\tilde{Y}^u = \left\{ \tilde{Y}_j^u \right\}_{j=1}^n$.

Cross pseudo-supervision. Supervise softmax predictions of DS with pseudo-labels of CS \hat{Y}^u and supervise softmax predictions of CS with pseudo-labels of DS \tilde{Y}^u :

$$L_p^d = D(\tilde{P}^u, \hat{Y}^u) + \lambda_1 E(\tilde{P}^u, \hat{Y}^u), \quad (6)$$

$$L_p^c = D(\hat{P}^u, \tilde{Y}^u) + \lambda_2 E(\hat{P}^u, \tilde{Y}^u), \quad (7)$$

where λ_1 and λ_2 are weights of L_p^d and L_p^c and

$$D(\tilde{P}^u, \hat{Y}^u) = 1 - \frac{2|\tilde{P}^u \cap \hat{Y}^u|}{|\tilde{P}^u| + |\hat{Y}^u|}, \quad (8)$$

$$E(\tilde{P}^u, \hat{Y}^u) = - \sum_{i=0}^{c-1} \hat{Y}_i^u \cdot \log(\tilde{P}_i^u), \quad (9)$$

where $D(\hat{P}^u, \tilde{Y}^u)$ and $E(\hat{P}^u, \tilde{Y}^u)$ are the same with them.

4.2. High-Frequency Mamba Module (HFM)

Medical images often display structured anatomical patterns with clear sequential relationships, where global contextual information is crucial for enhancing the extraction of fine details. To address the computational challenges faced by CNNs in capturing high-frequency details, we develop a 3D high-frequency Mamba module that leverages the global contextual information of the images to learn details of samples globally.

To obtain high-frequency components of features, 3D features are first transformed from the spatial domain to the frequency domain by the fast Fourier transform (FFT). Then, the features are filtered through high-pass filtering (HPF) to obtain high-frequency features. Finally, the obtained high-frequency features are transformed into the spatial domain for mamba attention learning. The process flow is shown in Figure 3.

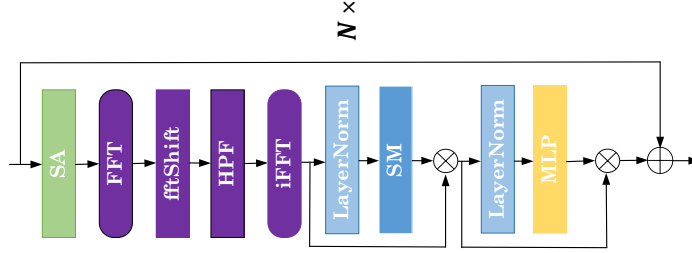


Figure 3: High-frequency mamba block.

The module is defined as follows:

$$\begin{aligned}
 F_g &= \text{FFT}(\text{SA}(\hat{f}^{l/u})) \\
 F_h &= \text{iFFT}(\text{HPF}(\text{fftShift}((F_g)))) \\
 F_m &= \text{SM}(\text{LN}(F_h)) + F_h \\
 F_o &= \text{MLP}(\text{LN}(F_m)) + F_m,
 \end{aligned} \tag{10}$$

where $\hat{f}^{l/u}$ denotes 3D labeled or unlabeled features of CS network. We adopt a Spatial Attention module (SA) and a Space Mamba (SM) introduced in [Xing et al. \(2024\)](#). `fftShift` represents spectrum centralization. `iFFT` is Fast Inverse Fourier transform. SM includes forward, backward, and space orientation for encoding 3D features. LN and MLP denote the Layer Normalization and Multiple Layers Perception Layer to enrich the feature representation.

4.3. Label Information Propagation by Contrastive Learning

Medical images typically exhibit consistent structures within the same class and significant differences between different classes. We believe that regions in unlabeled data similar to overall class semantics in labeled data are likely to belong to the same class, while regions with minimal similarity are less likely to. We uses contrastive learning to label information propagation by narrowing the boundaries between regions in unlabeled data similar to overall semantics of labeled data in each class and expand those between unrelated ones.

A memory bank (MB) is built to store pairs of labeled features from the DS and corresponding labels. Screen out the part that DS predicts correctly for labeled samples, and store the features of these pixels in MB. We randomly select p labeled features for each class from MB which represent

class semantics and get $\mathbf{a} = (\mathbf{a}^1, \mathbf{a}^2, \dots, \mathbf{a}^C)$, where $\mathbf{a}^\gamma = (a_1^\gamma, a_2^\gamma, \dots, a_p^\gamma)$, $\gamma \in \{1, \dots, C\}$, where C is the class number of a dataset. We randomly sample q unlabeled features $\mathbf{b} = (b_1, b_2, \dots, b_q)$ from all unlabeled features projected by CS.

Next, find out the unlabeled features that are semantically similar and unrelated to each class in labeled features from the unlabeled features \mathbf{b} . Calculate the cosine distance between each unlabeled feature in \mathbf{b} and each labeled feature in \mathbf{a}^γ :

$$\cos(b_j, a_i) = \frac{\sum_{w=1}^r a_i \cdot b_j}{\sum_{k=1}^r a_i \times \sum_{k=1}^r b_j}, \quad (11)$$

where $a_i \in \mathbf{a}^\gamma$ and $b_i \in \mathbf{b}$. r is the dimension of the feature. According to cosine similarity, find the top-k most similar and top-k least similar unlabeled features in \mathbf{b} to the labeled feature vector \mathbf{a} :

$$\mathbf{b}^{\gamma, P} = \max_{j=1}^k \sum_{i=1, a_i \in \mathbf{a}^\gamma}^p \cos(b_j, a_i), \quad (12)$$

$$\mathbf{b}^{\gamma, N} = \max_{j=1}^k \sum_{a_i \in \mathbf{a}^\gamma}^p (1 - \cos(b_j, a_i)), \quad (13)$$

Every feature in $\mathbf{b}^{\gamma, P}$ and $\mathbf{b}^{\gamma, N}$ are positive and negative pairs of labeled feature vector \mathbf{a}^γ , respectively. We can get $\{(\mathbf{b}^{1, P}, \mathbf{b}^{1, N}), \dots, (\mathbf{b}^{C, P}, \mathbf{b}^{C, N})\}$.

Contrastive learning narrows the distance between positive pairs and enlarges the distance between negative pairs. For $a_i \in \mathbf{a}^\gamma$ and $b_j \in \mathbf{b}^{\gamma, N}$, the contrastive loss between them is calculated as follows:

$$\mathcal{L}(a_i, b_j) = -\log \frac{e^{\cos(a_i, b_j)/\tau}}{e^{\cos(a_i, b_j)/\tau} + \sum_{\alpha=1, b_\alpha \in \mathbf{b}^{\gamma, N}}^k e^{\cos(a_i, b_\alpha)/\tau}}, \quad (14)$$

where $a_i \in \mathbf{a}^\gamma$ and $b_j \in \mathbf{b}^{\gamma, N}$. τ is a temperature parameter. Our label information propagation loss is defined as follows:

$$L_{cl} = \sum_{\gamma=1}^C \sum_{\{i=1, i \in \mathbf{a}^\gamma\}}^p \sum_{\{j=1, j \in \mathbf{b}^{\gamma, P}\}}^k \mathcal{L}(a_i, b_j). \quad (15)$$

Algorithm 1: Training Process of Diff-CL.

Input: CS $f^c(\cdot)$; DS $f^d(\cdot)$; Labeled dataset S^l ; Unlabeled dataset S^u ; the max iteration I

Output: Trained CS $f^c(\cdot)$ for inference

- 1: Initialize CS $f^c(\cdot)$ and DS $f^d(\cdot)$;
 - 2: **for** $epoch \leq I$ **do**
 - 3: Sampled batch data x^l and x^u from S^l and S^u ;
 - 4: CS Forward: $\hat{P}^l = f^c(x^l)$; $\hat{P}^u = f^c(x^u)$;
 - 5: Pseudo labels of CS:
 $\hat{Y}^l = \operatorname{argmax}(\hat{P}^l)$; $\hat{Y}^u = \operatorname{argmax}(\hat{P}^u)$;
 - 6: Add Noise by Eq. 5: y_t^l ; y_t^u ;
 - 7: DS Forward: $\tilde{P}^l = f^d(x^l, y_t^l)$; $\tilde{P}^u = f^d(x^u, y_t^u)$;
 - 8: Get supervised loss of CS by Eq. 19;
 - 9: Get supervised loss of DS by Eq. 18;
 - 10: Cross pseudo-supervision loss of CS by Eq. 7;
 - 11: Cross pseudo-supervision loss of DS by Eq. 6;
 - 12: Label information propagation loss by Eq. 15;
 - 13: Calculate loss L_u^c by Eq. 22;
 - 14: Update CS using Eq. 17;
 - 15: Update DS using Eq. 16;
 - 16: **end for**
-

4.4. Semi-supervised Training

The total objective function to train our DS-CS networks is both a weighted combination of a supervised loss on labeled data and an unsupervised loss on unlabeled data, defined as:

$$L^d = L_s^d + \mu_1 L_p^d, \quad (16)$$

$$L^c = L_s^c + \mu_2 L_u^c, \quad (17)$$

where L^d and L^c are the total losses of DS and CS, respectively. μ_1 and μ_2 are the weights to adjust ratios of cross pseudo-supervision loss for DS L_p^d and unsupervised loss for CS L_u^c , respectively.

The dice coefficient $D(\cdot)$ and cross-entropy $E(\cdot)$ guide the training for labeled data:

$$L_s^d = D(\tilde{P}^l, y^l) + \beta_1 E(\tilde{P}^l, y^l), \quad (18)$$

Table 2: Parameter Settings of Diff-CL on three datasets. μ_1 , μ_2 , β_1 , β_2 , λ_1 , λ_2 , and η are introduced in 4. HF is the threshold of high-frequency filters.

Dataset	Labeled/Unlabeled	Batch Size	μ_1	μ_2	β_1	β_2	λ_1	λ_2	η	HF
Pancreas	6/56	4	1	1	$0.1 \times \lambda(t)$	$0.1 \times \lambda(t)$	1	1	0.007	0.8
	12/50	4	1	1	$0.1 \times \lambda(t)$	$0.1 \times \lambda(t)$	1	1	0.0003	0.5
LA	4/76	4	1	1	$0.01 \times \lambda(t)$	$0.01 \times \lambda(t)$	1	1	0.7	0.6
	8/72	4	1	1	$0.01 \times \lambda(t)$	$0.01 \times \lambda(t)$	1	1	0.5	0.7
BraTS	25/225	4	1	1	$0.1 \times \lambda(t)$	$0.1 \times \lambda(t)$	1	1	0.007	0.5
	50/250	4	1	1	$0.1 \times \lambda(t)$	$0.1 \times \lambda(t)$	1	1	0.003	0.5

$$L_s^c = D(\hat{P}^l, y^l) + \beta_2 E(\hat{P}^l, y^l), \quad (19)$$

where β_1 and β_2 are the weights of cross entropy $E(\tilde{P}^l, y^l)$ and $E(\hat{P}^l, y^l)$ and

$$D(\tilde{P}^l, y^l) = 1 - \frac{2|\tilde{P}^l \cap y^l|}{|\tilde{P}^l| + |y^l|}, \quad (20)$$

$$E(\tilde{P}^l, y^l) = - \sum_{i=0}^{c-1} y_i^l \cdot \log(\tilde{P}_i^l), \quad (21)$$

where $D(\hat{P}^l, y^l)$ and $E(\hat{P}^l, y^l)$ are the same with them.

Cross pseudo supervision loss L_p^d and L_p^c in section 4.1 and inter-sample contrastive learning loss L_{cl} in section 4.3 guide the DS and CS training for unlabeled data, defined as:

$$L_u^c = L_p^c + \eta L_{cl}, \quad (22)$$

where η are weights of L_{cl} . The entire flow of Diff-CL is presented in Algorithm 1.

5. Experiments

5.1. Datasets and experimental setup

We evaluate the performances of Diff-CL on three publicly available datasets.

Left atrium segmentation dataset. 3D Left Atrium (LA) segmentation dataset Xiong et al. (2021) contains 100 3D gadolinium-enhanced MR Images with a resolution of $0.625mm \times 0.625mm \times 0.625mm$. The preprocessing procedure is the same as in (Luo et al. (2021); Li et al. (2020); Yu et

al. (2019); Xu et al. (2023); Gao et al (2023); Wu et al. (2021)) and we use 80 scans for training and 20 scans for testing. All images are cropped at the center of the heart region and normalized to zero mean and unit variance.

Brain tumor segmentation dataset: The brain tumor segmentation (BraTS) is from the BraTS 2019 challenge Spyridon (Spyros), containing preoperative MRI (with modalities of T1, T1Gd, T2, and T2-FLAIR) of 335 glioma patients, where 259 patients are with high-grade glioma (HGG) and 76 patients are with low-grade glioma (LGG). Like Xu et al. (2023), we use T2-FLAIR images in this task and segment the whole tumor region. The images are resampled to the isotropic resolution of $1 \times 1 \times 1$ mm³. Following the same data split and preprocessing procedure as in Xu et al. (2023), 250 samples are used for training, 25 for validation, and the remaining 60 for testing.

NIH pancreas dataset The NIH Pancreas Dataset (Pancreas) Roth et al. (2015) includes 82 contrast-enhanced abdominal 3D CT volumes with manual annotation. The size of each CT volume range from $512 \times 512 \times 181$ to $512 \times 512 \times 466$. Our preprocessing is like Luo et al. (2021). In our experiments, the soft tissue CT window we use is $[-120, 240]$ HU, and the CT scans are cropped centered at the pancreas region, and the margins are enlarged with 25 voxels. 62 volumes are used for training and 20 volumes are used for testing.

Metrics. We use four complementary evaluation metrics to quantitatively evaluate the segmentation performances of every model during the testing process, including the Dice similarity Index (Dice), Jaccard Index (Jaccard), Average surface distance (ASD), and 95% Hausdorff (95HD). Dice and Jaccard measure region matching, and higher Dice and Jaccard scores indicate higher pixel-level matching. ASD and 95HD are two boundary-based metrics that measure boundary differences in images, and lower ASD and 95HD scores indicate more minor boundary differences in images.

Baseline approaches. We compare Diff-CL with seven semi-supervised image segmentation methods: dual-task consistency (DTC) Luo et al. (2021), shape-aware model (SASSNet) Li et al. (2020), uncertainty-aware MT (UAMT) Yu et al. (2019), uncertainty rectified pyramid consistency (URPC) Luo et al. (2022), Mutual Consistency Network (MC-Net) Wu et al. (2021), MC-Net+ Wu et al. (2022), ambiguity-consensus mean-teacher (AC-MT) Xu et al. (2023), correlation-aware mutual learning (CAML) Gao et al (2023), and mutual learning with reliable pseudo label (ML-RPL) Su et al. (2024).

Implementation details. All the networks in our experiments are im-

Table 3: Results of quantitative comparison on LA dataset.

Method	Scans used		Metrics			
	Labeled/Unlabeled	Dice(%) \uparrow	Jaccard(%) \uparrow	95HD \downarrow	ASD \downarrow	
V-Net Milletari et al. (2016)	4/0	52.55	39.60	47.05	9.87	
DTC Luo et al. (2021)	4/76	82.75	71.55	13.77	3.91	
SASSnet Li et al. (2020)	4/76	83.26	71.92	15.51	4.63	
UA-MT Yu et al. (2019)	4/76	81.16	68.97	24.22	6.97	
URPC Luo et al. (2022)	4/76	83.47	72.56	14.02	3.68	
MC-Net Wu et al. (2021)	4/76	84.06	73.04	12.16	2.42	
MC-Net+ Wu et al. (2022)	4/76	83.13	71.58	12.69	2.71	
AC-MT Xu et al. (2023)	4/76	87.42	77.83	<u>9.09</u>	<u>2.19</u>	
CAML Gao et al. (2023)	4/76	<u>87.54</u>	<u>77.95</u>	10.76	2.58	
ML-RPL Su et al. (2024)	4/76	84.70	73.75	13.73	3.53	
Diff-CL (ours)	4/76	89.03	80.35	6.36	2.18	
V-Net Milletari et al. (2016)	8/0	78.57	66.96	21.20	6.07	
DTC Luo et al. (2021)	8/72	87.43	78.06	8.38	2.40	
SASSnet Li et al. (2020)	8/72	87.80	76.91	14.57	4.11	
UA-MT Yu et al. (2019)	8/72	84.48	73.98	17.13	4.82	
URPC Luo et al. (2022)	8/72	87.14	77.41	11.79	2.43	
MC-Net Wu et al. (2021)	8/72	88.99	80.32	<u>7.92</u>	<u>1.76</u>	
MC-Net+ Wu et al. (2022)	8/72	88.33	79.32	9.07	1.82	
AC-MT Xu et al. (2023)	8/72	88.74	79.94	8.29	1.91	
CAML Gao et al. (2023)	8/72	<u>89.44</u>	<u>81.01</u>	10.10	2.09	
ML-RPL Su et al. (2024)	8/72	87.35	77.72	8.99	2.17	
Diff-CL (ours)	8/72	91.00	83.54	5.08	1.68	
V-Net Milletari et al. (2016)	100%	91.62	84.60	5.40	1.64	

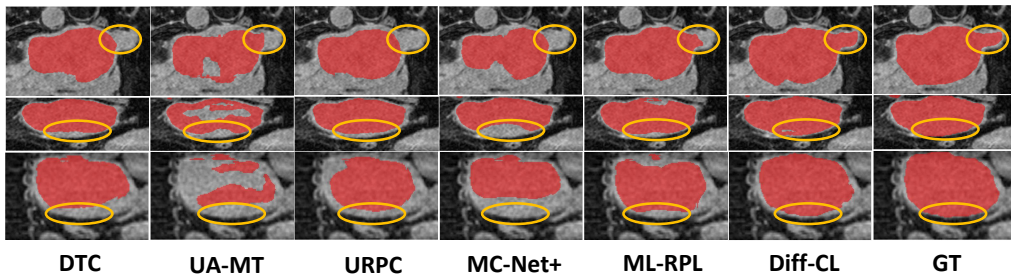


Figure 4: Results of qualitative comparison on LA dataset under 10% labeled data setting. GT represents the ground truth.

Table 4: Results in quantitative comparison on BraTS dataset.

Method	Scans used		Metrics		
	Labeled/Unlabeled	Dice(%) \uparrow	Jaccard(%) \uparrow	95HD \downarrow	ASD \downarrow
V-Net Milletari et al. (2016)	25/0	74.43	61.86	37.11	2.79
DTC Luo et al. (2021)	25/225	80.01	69.78	11.56	1.94
SASSnet Li et al. (2020)	25/225	77.44	66.24	21.55	6.77
UA-MT Yu et al. (2019)	25/225	82.82	72.42	14.01	3.75
URPC Luo et al. (2022)	25/225	<u>83.61</u>	<u>73.52</u>	<u>9.92</u>	<u>1.59</u>
MC-Net Wu et al. (2021)	25/225	83.33	73.29	<u>9.92</u>	2.42
MC-Net+ Wu et al. (2022)	25/225	82.18	72.18	10.81	1.74
AC-MT Xu et al. (2023)	25/225	81.60	71.04	10.76	2.06
CAML Gao et al (2023)	25/225	83.91	74.18	13.23	3.54
ML-RPL Su et al. (2024)	25/225	81.60	71.23	11.63	2.99
Diff-CL (ours)	25/225	84.63	75.05	12.08	3.73
V-Net Milletari et al. (2016)	50/0	80.13	70.15	14.83	4.28
DTC Luo et al. (2021)	50/200	81.17	70.96	11.51	2.16
SASSnet Li et al. (2020)	50/200	81.58	71.44	10.74	1.97
UA-MT Yu et al. (2019)	50/200	81.21	71.38	11.96	3.73
URPC Luo et al. (2022)	50/200	84.05	20.72	11.17	2.45
MC-Net Wu et al. (2021)	50/200	83.16	73.47	<u>8.68</u>	2.16
MC-Net+ Wu et al. (2022)	50/200	<u>84.10</u>	<u>74.56</u>	9.99	2.68
AC-MT Xu et al. (2023)	50/200	83.28	73.26	9.87	<u>1.79</u>
CAML Gao et al (2023)	50/200	81.94	72.17	9.86	2.85
ML-RPL Su et al. (2024)	50/200	80.49	70.07	15.65	4.73
Diff-CL (ours)	50/200	85.45	75.88	9.05	2.6
V-Net Milletari et al. (2016)	100%	86.4	77.43	6.98	1.79

plemented on a server with NVIDIA GeForce RTX 2080 10GB GPU, Pytorch 2.2.2+cu118, and Python 3.11. The training for DS and CS models both employ the Stochastic Gradient Descent (SGD) optimizer for 300 epochs, augmented with a weight decay of 3×10^{-5} and a momentum of 0.9, while the learning rate is maintained at 0.01. Gaussian warming up function is used to control the weight $\lambda(t) = 2.0 \times e^{-5(1-t/t_{max})^2}$, where t represents the current epoch, and $t_{max} = 300$. To mitigate overfitting, we augment the training dataset with random cropping, flipping, and rotation techniques. For seg-

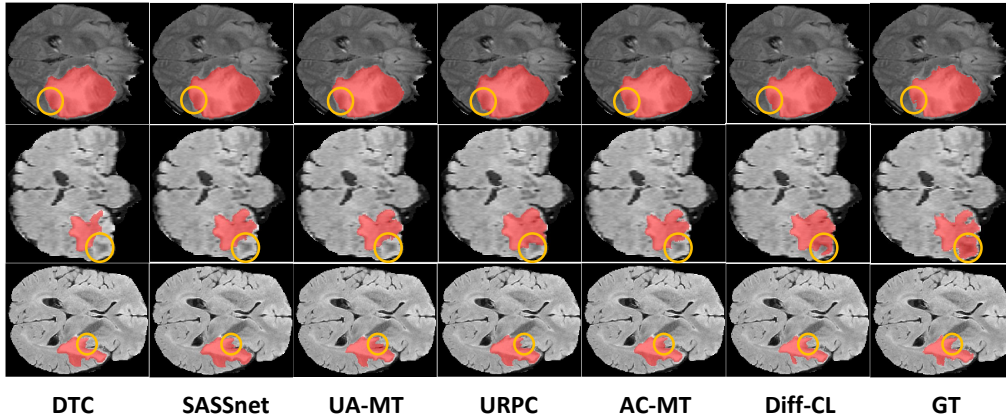


Figure 5: Results of quantitative comparison on BraTS dataset. GT represents the ground truth.

mentation tasks, we utilize V-Net [Milletari et al. \(2016\)](#) as the backbone network of DS and CS. In LA segmentation, input patches are randomly cropped to dimensions of $112 \times 112 \times 80$ voxels, with predictions made using a sliding window strategy with strides of $18 \times 18 \times 4$ voxels. For Pancreas and BraTS segmentation, patches are randomly cropped to $96 \times 96 \times 96$ voxels, and predictions are similarly performed using a sliding window approach with strides of $16 \times 16 \times 16$ and $64 \times 64 \times 64$ voxels, respectively.

5.2. Experimental results

We give quantitative and qualitative analysis for segmentation results on three datasets. All experiments on LA, BraTS, and Pancreas datasets use V-Net architecture.

5.2.1. Experiments on left atrium segmentation

We conduct comparative experiments on LA dataset under 5% and 10% labeled data settings, respectively.

As shown in [Table 3](#), Diff-CL outperforms nine other methods across three different labeled data settings. Compared nine current methods, under 5% labeled data setting, Diff-CL exceeds the highest Dice score by 1.49%, Jaccard score by 2.4%, and has 3.54 lower 95HD and 0.01 lower ASD than the best alternatives. Under 10%, Diff-CL is 1.56% higher in Dice, 2.53% higher in Jaccard, 2.84 lower in 95HD, and 0.08 lower in ASD. These results indicate

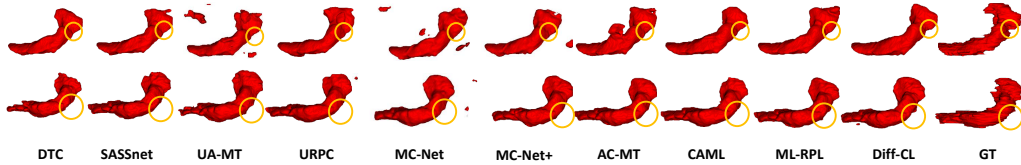


Figure 6: Results of qualitative comparison on Pancreas dataset under 10% labeled data setting. GT represents the ground truth.

the effectiveness of Diff-CL and its near-supervised performance even with limited labeled data.

As shown in Fig. 4, in the highlighted areas, segmentation of Diff-CL aligns more closely with the Ground Truth, even with only 10% labeled data. Compared to methods like UA-MT and MC-Net+, Diff-CL better preserves atrial edges and details, demonstrating efficient use of limited labeled data and strong performance across various labeling ratios.

5.2.2. BraTS segmentation dataset

We conduct comparative experiments on BraTS dataset under 10% and 20% labeled data settings.

As shown in Table 4, Dice score (84.63%) of Diff-CL improved by 1.02% over URPC, and its Jaccard index (75.05%) increased by 1.53% under 10% labeled data setting. Dice score (85.45%) of Diff-CL improved by 1.35% over URPC, and its Jaccard index (75.88%) increased by 1.32% under 20% labeled data setting. However, similar to results on pancreas dataset, 95HD and ASD was at the middle level of all methods on BraTS dataset. These results indicate that Diff-CL has significant advantages in accuracy prediction, however, it needs to pay more attention to the boundary.

As shown in Fig. 5, the segmentation of first and third samples by Diff-CL is more accurate in detail than that by other methods in blue box. In the second sample, other methods did not segment the foreground area in blue box, and the shape of Diff-CL is more similar to ground truth.

5.2.3. Experiments on NIH pancreas segmentation

We conduct comparative experiments on the pancreas dataset under 10% and 20% labeled data settings.

In Table 5, under 10% labeled data setting, Diff-CL achieves a Dice score of 78.21% and a Jaccard index to 64.80%, which is 0.26% and 0.27% higher than the best of 77.95% and 64.53% by ML-RPL, respectively. Under 20%

Table 5: Results in quantitative comparison on Pancreas dataset.

Method	Scans used		Metrics			
	Labeled/Unlabeled	Dice(%) \uparrow	Jaccard(%) \uparrow	95HD \downarrow	ASD \downarrow	
V-Net Milletari et al. (2016)	6/0	60.39	46.17	24.94	2.23	
DTC Luo et al. (2021)	6/56	69.01	54.52	20.99	2.33	
SASSnet Li et al. (2020)	6/56	72.28	58.06	14.30	2.45	
UA-MT Yu et al. (2019)	6/56	71.26	56.15	22.01	7.36	
URPC Luo et al. (2022)	6/56	72.66	18.99	22.63	6.36	
MC-Net Wu et al. (2021)	6/56	69.96	55.57	23.90	1.56	
MC-Net+ Wu et al. (2022)	6/56	63.31	49.15	31.99	2.09	
AC-MT Xu et al. (2023)	6/56	73.00	58.93	18.36	1.91	
CAML Gao et al (2023)	6/56	70.33	55.85	20.60	<u>1.71</u>	
ML-RPL Su et al. (2024)	6/56	<u>77.95</u>	<u>64.53</u>	<u>8.77</u>	2.29	
Diff-CL (ours)	6/56	78.21	64.8	14.11	3.26	
V-Net Milletari et al. (2016)	12/0	71.52	57.68	18.12	5.41	
DTC Luo et al. (2021)	12/50	73.55	59.90	13.55	1.59	
SASSnet Li et al. (2020)	12/50	77.43	64.18	11.78	1.53	
UA-MT Yu et al. (2019)	12/50	76.66	63.09	11.85	3.53	
URPC Luo et al. (2022)	12/50	75.22	22.75	13.86	4.06	
MC-Net Wu et al. (2021)	12/50	74.80	60.57	19.18	4.64	
MC-Net+ Wu et al. (2022)	12/50	73.71	60.34	13.93	4.00	
AC-MT Xu et al. (2023)	12/50	78.86	66.02	<u>7.98</u>	1.47	
CAML Gao et al (2023)	12/50	74.96	61.81	14.60	<u>1.29</u>	
ML-RPL Su et al. (2024)	12/50	<u>80.29</u>	<u>67.53</u>	9.50	2.21	
Diff-CL (ours)	12/50	81.27	68.87	9.32	2.16	
V-Net Milletari et al. (2016)	100%	82.60	70.81	5.61	1.33	

labeled data setting, Diff-CL achieves a Dice score of 81.27% and a Jaccard index to 68.87%, which is 0.98% and 1.34% significantly higher than the best of 80.29% and 67.53% by ML-RPL, respectively, which demonstrate superior segmentation accuracy. However, 95HD and ASD are not the best of all these methods, so Diff-CL must further improve the boundary precision on pancreas dataset.

As shown in Fig. 6, in the first row, within the blue circle, Diff-CL identifies the furrow, while other methods fail to detect it. In the second row, within the blue circle, Diff-CL successfully segments a synapse that closely resembles the ground truth (GT), whereas the other methods miss

Table 6: Ablation studies on Pancreas and LA datasets under 5%, 10% and 20% labeled data setting respectively.

Methods				Metrics			
$L_s^c + L_s^d$	$L_p^c + L_p^d$	HFM	L_{cl}	Dice(%)	Jaccard(%)	95HD	ASD
Pancreas Dataset							
✓				71.52	57.68	18.12	5.41
✓	✓			80.36	67.81	8.85	2.00
✓	✓	✓		80.85	68.32	9.75	2.62
✓	✓	✓	✓	81.27	68.87	9.32	2.16
LA Dataset							
✓				84.81	76.48	8.84	2.14
✓	✓			86.54	77.70	6.02	2.26
✓	✓	✓		88.17	79.23	8.23	2.8
✓	✓	✓	✓	89.02	80.34	6.32	2.16

this segment altogether. This highlights the superior capability of Diff-CL in accurately capturing fine structures that other methods overlook.

5.3. Ablation study

We have done ablation studies to verify the effectiveness of Diff-CL. Table 6 presents results of ablation studies on three datasets: Pancreas and LA. We compare different combinations of loss functions and evaluate their impact on various metrics: Dice, Jaccard, 95HD, and ASD. Using only supervised loss including L_s^c and L_s^d provides a solid foundation for segmentation accuracy but leaves room for improvement in boundary approximation and segmentation smoothness. Adding cross-pseudo-supervision losses L_p^c and L_p^d and the high-frequency mamba (HFM) module significantly improves segmentation accuracy and overlap (Dice and Jaccard). It also enhances boundary approximation and smoothness, as evidenced by lower 95HD and ASD values. Including inter-sample contrastive loss yields the highest accuracy and best overlap (Dice and Jaccard) among all setups. It also substantially reduces the worst-case boundary error (95HD) and improves contour smoothness (ASD). This research shows the effectiveness of Diff-CL.

6. Conclusion

This paper proposes a new semi-supervised medical image segmentation framework from the distribution perspective. On the one hand, we propose

a cross-pseudo-supervision learning mechanism of diffusion and convolution segmentation networks. Combining diffusion models with convolutional neural networks enables the former to learn data distribution while the latter corrects fine details. Consider capturing complete high-frequency details by CNNs requires substantial computational resources and is susceptible to local noise, we design a 3D high-frequency Mamba module to learn high-frequency details in medical images. On the other hand, given that both labeled and unlabeled data come from the same distribution, we utilize contrastive learning to verify our idea that regions in unlabeled data similar to overall class semantics to labeled data are likely to belong to the same class, while regions with minimal similarity are less likely to. The superior segmentation performance on the NIH pancreas, left atrium, and brain tumor datasets demonstrate the effectiveness of Diff-CL.

Declaration of interests

The authors declare that they have no known competing financial interests or personal relationships that could have appeared to influence the work reported in this paper.

Data availability

Data will be available upon request.

Acknowledgments

This work was supported by National Natural Science Foundation of China Grants (No.12101426 and No.12426308), Beijing Outstanding Young Scientist Program (No. JWZQ20240101027), and Beijing Natural Science Foundation Grants (No.Z210003 and No.4254093).

References

Bai, W., Oktay, O., Sinclair, M., Suzuki, H., Rajchl, M., Tarroni, G., Glocker, B., King, A., Matthews, P. M, Rueckert, D., Sept. 2017. Semi-supervised learning for network-based cardiac MR image segmentation. In: Proceedings of Medical Image Computing and Computer Assisted Intervention. pp. 253-260.

- Basak, H., Yin, Z., 2023. Pseudo-label guided contrastive learning for semi-supervised medical image segmentation. In: Proceedings of the IEEE/CVF conference on computer vision and pattern recognition. pp. 19786-19797.
- Dong-DongChen, W., WeiGao, Z. H., 2018. Tri-net for semi-supervised deep learning. In: Proceedings of twenty-seventh international joint conference on artificial intelligence. pp. 2014-2020.
- Fan, C., Yu, H., Wang, L., Huang, Y., Wang, L., Jia, X., 2024. SliceMamba for Medical Image Segmentation. preprint arXiv: 2407.08481.
- Gao, S., Zhang, Z., Ma, J., Li, Z., Zhang, S., Oct. 2023. Correlation-aware mutual learning for semi-supervised medical image segmentation. In: Proceedings of Medical Image Computing and Computer Assisted Intervention. pp. 98-108.
- Gu, A., Dao, T., 2023a. Mamba: Linear-time sequence modeling with selective state spaces. arXiv preprint arXiv:2312.00752.
- Gu, A., 2023b. Modeling sequences with structured state spaces, Ph.D. thesis, Stanford University. <https://purl.stanford.edu/mb976vf9362>.
- Gu, A., Goel, K., Re, C. 2022. Efficiently modeling long sequences with structured state spaces. arXiv preprint arXiv:2111.00396.
- Iscen, A., Tolia, G., Avrithis, Y., Chum, O., 2019. Label propagation for deep semi-supervised learning. In: Proceedings of the IEEE/CVF conference on computer vision and pattern recognition. pp. 5070-5079.
- Lai, X., Tian, Z., Jiang, L., Liu, S., Zhao, H., Wang, L., Jia, J., 2021. Semi-supervised semantic segmentation with directional context-aware consistency. In: Proceedings of the IEEE/CVF Conference on Computer Vision and Pattern Recognition. pp. 1205–1214.
- Lei, T., Zhang, D., Du, X., Wang, X., Wan Y., Nandi, A. K., May 2023. Semi-Supervised Medical Image Segmentation Using Adversarial Consistency Learning and Dynamic Convolution Network. IEEE Trans. Med. Imag. 42, 5, 1265-1277.
- Li, S., Zhang, C., He, X., 2020. Shape-aware semi-supervised 3D semantic segmentation for medical images. In: Proceedings of Medical Image Computing and Computer Assisted Intervention. pp. 552–561.

- Liu, X., Li, W., Yuan, Y., Dec. 2023. Towards Generic Semi-Supervised Framework for Volumetric Medical Image Segmentation. *Adv. Neural Inf. Process Syst.* 36.
- Liu, X., Li, W., Yuan, Y., Sept. 2024. DiffRect: Latent Diffusion Label Rectification for Semi-supervised Medical Image Segmentation. In: *Proceedings of International Conference on Medical Image Computing and Computer-Assisted Intervention*. Springer, pp. 56-66.
- Liu, Z., Lin, Y., Cao, Y., Hu, H., Wei, Y., Zhang, Z., Lin, S., Guo, B., 2021. Swin transformer: Hierarchical vision transformer using shifted windows. In: *Proceedings of the IEEE/CVF international conference on computer vision*. pp. 10012-10022.
- Luo, X., Chen, J., Song, T. Wang, G., 2021. Semi-supervised medical image segmentation through dual-task consistency. In: *Proceedings of the AAAI conference on artificial intelligence*. 35, 10, 8801–8809.
- Luo, X., Wang, G., Liao, W., Chen, J., Song, T., Chen, Y., Zhang, S., Metaxas, D. N, and Zhang, S., 2022. Semi-supervised medical image segmentation via uncertainty rectified pyramid consistency. *Med. Image Anal.* 80, 102517.
- Liu, Y., Tian, Y., Zhao, Y., Yu, H., Xie, L., Wang, Y., Ye, Q., Liu, Y., 2024. Vmamba: Visual state space model. *arXiv preprint arXiv:2401.10166*.
- Milletari, F., Navab, N., Ahmadi, S.A., 2016. V-Net: Fully convolutional neural networks for volumetric medical image segmentation. In: *Fourth International Conference on 3D Vision*. IEEE, pp. 565–571.
- Peng, H., Chen, S., Niu, N., Wang, J., Yao, Q., Wang, L., Wang, Y., Tang, J., Wang, G., Huang, M., Xue, C., 2023. Diffusion Model in Semi-Supervised Scleral Segmentation. In: *IEEE International conference on pattern recognition and artificial intelligence*. pp. 376-382.
- Peng, J., Estrada, G., Pedersoli, M., Desrosiers C., 2020. Deep co-training for semi-supervised image segmentation. *Pattern Recognit.* 107, 107269.
- Rajchl, M., Lee, M. C. H., Oktay, O., Kamnitsas, K., Passerat-Palmbach, J., Bai, W., Damodaram, M., Rutherford, M. A, Hajnal, J. V, Kainz, B., Rueckert, D., 2017. DeepCut: object segmentation from bounding box

- annotations using convolutional neural networks. *IEEE Trans. Med. Imag.* 36, 2, 674-683.
- Ronneberger, O., Fischer, P., Brox, T., 2015. U-Net: Convolutional networks for biomedical image segmentation. In: *Proceedings of International Conference on Medical Image Computing and Computer-Assisted Intervention*. Springer, pp. 234–241.
- Roth, H. R, Lu, L., Farag, A., Shin, H., Liu, J., Turkbey, E. B, Summers, R. M, 2015. Deeporgan: Multi-level deep convolutional networks for automated pancreas segmentation. In: *Proceedings of International Conference on Medical Image Computing and Computer-Assisted Intervention*. Springer, pp. 556-564.
- Ruan, J., Xiang, S., 2024. Vm-unet: Vision mamba unet for medical image segmentation. *arXiv preprint arXiv:2402.02491*.
- Seibold, C.M., Reiß, S., Kleesiek, J., Stiefelhagen, R., 2022. Reference-guided pseudo-label generation for medical semantic segmentation. In: *Proceedings of the AAAI conference on artificial intelligence*. 36, 2, 2171–2179.
- Song, J., Meng, C., and Ermon, S., 2020. Denoising diffusion implicit models. *arXiv preprint arXiv:2010.02502*.
- Song, Y., Zhang, C., Lee, J., Wang, F., Xiang, S., Zhang, D., 2009. Semi-supervised discriminative classification with application to tumorous tissues segmentation of MR brain images. *Pattern Anal. appl.* 12, 99-115.
- Spyridon (Spyros) Bakas, 2020. BraTS MICCAI brain tumor dataset. <http://dx.doi.org/10.21227/hdtd-5j88>.
- Su, J., Luo, Z., Lian, S., Lin, D., and Li, S., 2024. Mutual learning with reliable pseudo label for semi-supervised medical image segmentation. *Med. Image Anal.* 94, 103111.
- Tang, M., Valipour, S., Zhang, Z., Cobzas, D., Jagersand M., Sept. 2017. A deep level set method for image segmentation. In *Proceedings of Deep Learning in Medical Image Analysis and Multimodal Learning for Clinical Decision Support*. Springer, pp. 126-134.

- Wang, J., Zhu, W., Wang, P., Yu, X., Liu, L., Omar, M., Hamid, R., 2023. Selective structured state-spaces for long-form video understanding, in: Proceedings of the IEEE/CVF Conference on Computer Vision and Pattern Recognition. pp. 6387–6397.
- Wang, Z., Ma, C., 2024. Weak-mamba-unet: Visual mamba makes cnn and vit work better for scribble-based medical image segmentation. arXiv preprint arXiv:2402.10887.
- Wu, Y., Ge, Z., Zhang, D., Xu, M., Zhang, L., Xia, Y., Cai, J., 2022. Mutual consistency learning for semi-supervised medical image segmentation. *Med. Image Anal.* 81, 102530.
- Wu, Y., Xu, M., Ge, Z., Cai, J., Zhang, L., 2021. Semi-supervised left atrium segmentation with mutual consistency training. In: Proceedings of Medical Image Computing and Computer Assisted Intervention. pp. 297–306.
- Xia, Y., Yang, D., Yu, Z., Liu, F., Cai, J., Yu, L., Zhu, Z., Xu, D., Yuille, A., Roth, H., 2020. Uncertainty-aware multi-view co-training for semi-supervised medical image segmentation and domain adaptation. *Med. Image Anal.* 65, 101766.
- Xing, Z., Ye, T., Yang, Y., Liu, G., Zhu, L., 2024. Segmamba: Long-range sequential modeling mamba for 3d medical image segmentation. In: Proceedings of International Conference on Medical Image Computing and Computer-Assisted Intervention. Springer, pp. 578-588.
- Xiong, Z., Xia, Q., Hu, Z., Huang, N., Bian, C., Zheng, Y., Vesal, S., Ravikumar, N., Maier, A., Yang, X., Heng, P., Ni, D., Li, C., Tong, Q., Si, Q., Puybareau, E., Khoudli, Y., Géraud, T., Chen, C., Bai, W., Rueckert, D., Xu, L., Zhuang, X., Luo, X., Jia, S., Sermesant, M., Liu, Y., Wang, K., Borra, D., Masci, A., Corsi, C., Vente, C. d., Veta, M., Karim, R., Preetha, C. J., Engelhardt, S., Qiao, M., Wang, Y., Tao, Q., Nuñez-Garcia, M., Camara, O., Savioli, N., Lamata, P., Zhao, J., 2021. A global benchmark of algorithms for segmenting the left atrium from late gadolinium-enhanced cardiac magnetic resonance imaging. *Med. Image Anal.* 67, 101832.
- Xu, K., Su, H., Zhu, J., Guan, J. S., Zhang, B., 2016. Neuron segmentation based on CNN with semi-supervised regularization. In: Proceedings of IEEE conference on computer vision and pattern recognition. pp. 20-28.

- Xu, Z., Wang, Y., Lu, D., Luo, X., Yan, J., Zheng, Y., Tong, R. K., 2023. Ambiguity-selective consistency regularization for mean-teacher semi-supervised medical image segmentation. *Med. Image Anal.* 88, 102880.
- Yang, Z., Yan, Z., Diao, W., Zhang, Q., Kang, Y., Li, J., Li, X., Sun, X., 2023. Label propagation and contrastive regularization for semi-supervised semantic segmentation of remote sensing images. *IEEE Trans. Geosci. Remote Sens.* 61, 1-18.
- Yao, Y., Duan, X., Qu, A., Chen, M., Chen, J., Chen, L., 2024. DFCG: A Dual-Frequency Cascade Graph model for semi-supervised ultrasound image segmentation with diffusion model. *Knowl. Based Syst.* 300, 112261.
- You, C., Zhou, Y., Zhao, R., Staib, L., Duncan, J. S., 2022. SimCVD: Simple contrastive voxel-wise representation distillation for semi-supervised medical image segmentation. *IEEE Trans. Med. Imag.* 41, 9, 2228–2237.
- Yu, L., Wang, S., Li, X., Fu, C.-W., Heng, P.-A., 2019. Uncertainty-Aware Self-ensembling Model for Semi-supervised 3D Left Atrium Segmentation. In: *Proceedings of Medical Image Computing and Computer Assisted Intervention*. pp. 605-613.
- Zhao, X., Qi, Z., Wang, S., Wang, Q., Wu, X., Mao, Y., Zhang, L., 2023. Rcps: Rectified contrastive pseudo supervision for semi-supervised medical image segmentation. *IEEE J. Biomed. Health. Inf.*
- Zheng, Y., Wang, B., Hong, Q., 2022. UGAN: Semi-supervised Medical Image Segmentation Using Generative Adversarial Network. In: *International Congress on Image and Signal Processing, BioMedical Engineering and Informatics*. pp. 1-6.
- Zhong, Y., Yuan, B., Wu, H., Yuan, Z., Peng, J., Wang, Y.-X., 2021. Pixel contrastive-consistent semi-supervised semantic segmentation. In: *Proceedings of the IEEE/CVF International Conference on Computer Vision*. pp. 7273–7282.
- Zhou, Y., Wang, Y., Tang, P., Bai, S., Shen, W., Fishman, E., Yuille, A., Jan. 2019. Semi-supervised 3D abdominal multi-organ segmentation via deep multi-planar co-training. In: *IEEE Winter Conference on Applications of Computer Vision*. pp. 121-140.

Zou, S., Zhang, M., Fan, B., Zhou, Z., Zou, X., 2024. SkinMamba: A Precision Skin Lesion Segmentation Architecture with Cross-Scale Global State Modeling and Frequency Boundary Guidance. arXiv preprint arXiv:2409.10890.